Coherent Multiphoton Photoelectron Emission from Single Au Nanorods: The Critical Role of Plasmonic Electric Near-Field Enhancement

Andrej Grubisic, Volker Schweikhard, Thomas A. Baker, and David J. Nesbitt*

JILA, University of Colorado and National Institute of Standards and Technology, and Department of Chemistry and Biochemistry, University of Colorado, Boulder, Colorado 80309-0440, United States

ABSTRACT Electron emission from individual Au nanorods deposited on indium–tin–oxide (ITO) following excitation with femtosecond laser pulses near the rod longitudinal plasmon resonance is studied *via* scanning photoionization microscopy. The measured electron signal is observed to strongly depend on the excitation laser polarization and wavelength. Correlated secondary electron microscopy (SEM) and dark-field microscopy (DFM) studies of the same nanorods unambiguously confirm that maximum electron emission results from (i) laser polarization aligned with the rod long axis and (ii) laser wavelength resonant with the localized surface plasmon resonance. The experimental results are in good agreement with quantitative predictions for a coherent multiphoton photoelectric effect, which is identified as the predominant electron emission mechanism for metal nanoparticles under employed excitation conditions. According to this mechanism, the multiphoton photoemission rate is increased by over 10 orders of magnitude in the vicinity of a localized surface plasmon resonance, due to enhancement of the incident electromagnetic field in the particle near-field. These findings identify multiphoton photoemission as an extremely sensitive metric of local electric fields (*i.e.*, "hot spots") in plasmonic nanoparticles/structures that can potentially be exploited for direct quantitation of local electric field enhancement factors.

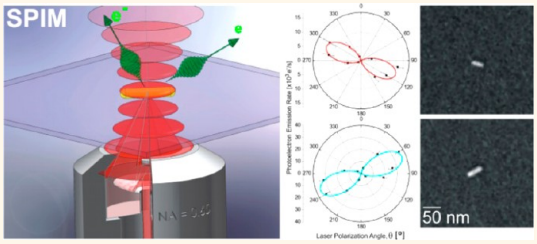

KEYWORDS: coherent multiphoton photoelectron emission · single-particle dark-field scattering · scanning photoionization microscopy · localized surface plasmon resonance · Au nanorods · ultrafast excitation

Optical extinction spectra of metallic nanoparticles often exhibit resonances in spectral regions where none exist in the bulk metal. These resonances arise due to localized surface plasmons (LSPs), which refer to excitations of a collective oscillation of conduction electrons confined within the nanoparticle volume.[1] For nanoparticles of the coinage metals (Cu, Ag, Au), such a plasmon oscillation (*i.e.*, resonance) occurs in the visible wavelength range, making these particles especially interesting for possible photonic applications. In addition, both size and shape of the nanoparticle are known to exert a profound effect on the plasmonic behavior.[2−5] Indeed, with the explosion of synthetic routes now available for generation of particles with well-defined sizes and shapes, the optical response of plasmonic features can be tuned throughout the visible spectral range and beyond.[6−12] This in turn has stimulated exciting proposals for use of metallic nanoparticles in a variety of novel applications, ranging from (i) solar cell absorbers,[13−16] (ii) subdiffraction-limited light guides in plasmonic devices,[17−19] (iii) photothermal anticancer agents in medicine,[20−22] (iv) high density storage bits in information technology,[23] and (v) ultrasensitive chemical detectors.[24−31]

In addition to affecting the optical properties of metallic nanoparticles, localized surface plasmons critically influence electron emissive behavior of particles as well. For example, in early studies of the surface photoelectric effect, one-photon (linear) photoemission spectra of metals were often dominated by a strong plasmon-induced electron emission peak that arose due to nanoscale surface roughness.[32−37] With the advent of ultrafast lasers, access to high laser intensities allowed plasmonic effects to also be observed in multiphoton (nonlinear)

* Address correspondence to djn@jila.colorado.edu.

Received for review May 27, 2012 and accepted November 29, 2012.

Published online November 29, 2012
10.1021/nn305194n

photoelectron emission (MPPE) from metal nanoparticle ensembles[38−42] and metallic nanostructures.[43,44] However, the inherent sensitivity of nonlinear phenomena on particle morphology leads to measured multiphoton photoemissivities to be dominated by contributions from only a few highly active particles/sites. As a result, ensemble-averaged techniques often underestimate nonlinear properties of nanoparticle systems and consequently make it challenging to investigate the influence of plasmons in multiphoton processes. This is particularly critical given the rapid growth of MPPE-based applications, such as (i) bright low-emittance sources of ultrashort electron pulses,[45,46] (ii) production of THz radiation,[47] (iii) high-harmonic generation,[48] and (iv) coherent control on the nanoscale,[49,50] to name a few.

To avoid such sample heterogeneity, several recent studies have focused on multiphoton photoelectron emission from individual plasmonic nanosystems and have observed tremendous particle-to-particle (or site-to-site) variations in photoemissivities.[44,51−60] These investigations established the critical role of plasmons in electron emission; however, details on how the LSP facilitates the photoemission process for nanoparticles remain of considerable interest and debate. Studies on flat metal surfaces have identified the coherent multiphoton photoelectric effect as the dominant electron emission mechanism for ultrafast excitation at photon energies ($E_{h\nu}$) below the metal work function (Φ).[61−67] In MPPE, a conduction electron within the metal coherently absorbs multiple photons to overcome the material work function and thus be emitted. According to this mechanism, the large plasmon-induced increase of photoemission yield observed in metal nanoparticles is attributed to local electric field enhancement arising from resonant excitation of a plasmon mode. While supporting evidence for this correspondence stems from beautiful work on Ag crescents,[54] Au nanostars,[53] and most recently Au nanoparticles on a metal plane,[55] direct experimental confirmation has been elusive because of the lack of independent methods for correlating photoemission and near-electric field enhancement.

Typically, the role of the electric near-field in photoelectron emission from metal nanoparticles is explored *via* correlations between plasmonic far- and near-field signatures in scattering and photoemission spectra, respectively. However, in stark contrast to metal surfaces, peak photoemission (a near-field phenomenon) for nanoparticles may not necessarily coincide with peak absorption and/or scattering (both far-field phenomena).[68−70] In fact, the wavelength for maximum electric near-field enhancement is generally redshifted compared to peaks in far-field quantities, presumably due to plasmon damping.[71] Furthermore, even far-field absorption and scattering properties may differ spectrally, since the localized surface plasmon decoheres *via* two competing pathways, that is, electron−electron scattering (light absorption) and radiative decay (light scattering), whose relative contributions depend on particle size and shape.[72] Such complications make rigorous comparison between far- and near-field properties of a single nanoparticle potentially quite challenging.

In this work, we focus on a well-defined nanoparticle system with well controlled excitation conditions (laser polarization, wavelength, intensity, pulse duration), which allows (i) unambiguous correlation between electric field enhancement and multiphoton photoemission yield and (ii) benchmark experimental photoemission rates for comparison with theoretical predictions. A wealth of information about the plasmonic response of Au nanorods makes them an ideal system in the present study for two reasons. First, they exhibit a longitudinal LSP resonance along the rod long axis, excited solely by the collinear electric field component and tunable from the visible to near-infrared (NIR) spectral region by rod aspect ratio (AR).[73] Second, weak longitudinal plasmon damping in Au nanorods results in nearly coincident absorption, scattering, and electric near-field enhancement spectra in the relevant wavelength range.[72] Consequently, the near- and far-field signatures of the longitudinal LSP should overlap, thus allowing the direct correlation between photoemission, light scattering, and E-field enhancement to be demonstrated at the single-particle level.

To confirm these expectations, correlated (i) scanning photoionization microscopy (SPIM),[51,52] (ii) dark-field microscopy (DFM), and (iii) secondary electron microscopy (SEM) are combined to study photoemissive, optical, and structural properties of single nanoparticles. The critical role of LSP in electron emission is further revealed through comparison of the experimental results with predictions of a coherent multiphoton photoemission model recently proposed by Yalunin *et al.*[74] Combined with numerical simulations of the particle near-electric field, these studies (i) offer insight into the dominant factor(s) influencing multiphoton photoemission, as well as (ii) benchmark theory against experiment for quantitation of electric near-field enhancements in more complex plasmonic nanostructures.

RESULTS

For the present study, Fourier-transform limited laser pulses ($\tau_P \approx 40$ fs) in the $\lambda = 720-890$ nm range ($E_{h\nu} = 1.39-1.72$ eV) are focused to a diffraction limited spot (full width half-maximum, fwhm = $0.515 \times \lambda/\mathrm{NA}$ = 634 nm for $\lambda = 800$ nm and objective numerical aperture NA = 0.65), yielding typical pulse energies of E_P = 0.2 pJ and $I = 6 \times 10^8$ W/cm^2 laser intensities. At these intensity levels, the smaller and larger Au nanorods are estimated to exhibit maximal peak temperatures of $T \approx 500$ and 400 K, respectively.[75,76] While previous studies suggest that elevated temperatures ($T \approx 500$ K)

for prolonged periods may cause particle melting/deformation, transient heating to even higher temperatures during an ultrafast pulse has been shown to induce little to no structural rearrangements.[75,77] This is also confirmed by our experiment; that is, we observe no change in the electron emission signal from single nanoparticles on the typical measurement time scale (*i.e.*, several minutes).

A typical SPIM image can be thought of as a 2D "map" of local electron emissivity. Sample data for the smaller Au nanorods (Sample I) on ITO are shown in Figure 1a and Figure 1b, where linear and logarithmic color scales are used, respectively. These images are recorded with circularly polarized light, in order to eliminate any potential dependence of photoemission signal on laser polarization. The regions of enhanced photoemissivity originate from individual Au nanorods, as clearly demonstrated *via* correlated SPIM (Figure 1c) and SEM (Figure 1d) images of the same sample area. Under typical excitation conditions, peak photoemission rates as high as 10^4 e^-/s are measured with nearly zero background signal from ITO (<0.1 e^-/s), resulting in a remarkably high signal-to-background ratio (S/B > 10^5) for a single-particle photoemission technique. Owing to the multiple photon nature of the excitation, one expects subdiffraction limited spot sizes governed by $w_n \approx w_1/\sqrt{n}$, where $w_1 = 0.515 \times \lambda/\mathrm{NA}$ is the fwhm anticipated for 1-photon absorption and n is the order of the photoemission process. Specifically, previous SPIM studies under similar laser excitation conditions support that photoemission from Au nanorods on ITO is a third order ($n = 3$) process.[52,59] The experimentally observed spot size ($w_3 \approx 280(70)$ nm) is in reasonable agreement with the expected value of $w_3 \approx w_1/\sqrt{3} = 366(10)$ nm.

Plasmon Directionality. The effect of laser polarization is indicated in a sequence of SPIM images in Figure 2a, recorded at $\lambda = 800$ nm and as a function of linear polarization angle, θ. Signals from three nanorods can be readily distinguished, one exhibiting peak photoemissivity at the laser polarization angle $\theta_0 \approx 120°$ and the other two near $\theta_0 \approx 60°$. Photoemission from individual rods can be observed only for laser polarization within a relatively narrow window (±60°) around θ_0. Indeed, the photoemission rate from a Au nanorod at a laser polarization perpendicular (±90°) to θ_0 is so small that it cannot be distinguished from ITO background, that is, in excess of a 10^5 contrast ratio. These observations confirm that Au nanorod photoemission occurs only for laser polarization aligned with a single particle direction. Specifically, the photoemission rate (N_{PE}) is modeled by $N_{PE} = A\cos^{2n}(\theta - \theta_0)$, where A denotes peak photoemissivity, n is the order of the photoemission process, and θ_0 is the laser polarization direction resulting in maximum photoelectron emission. Measured photoemission rates as a function of the laser polarization for two marked nanorods in Figure 2a are shown in polar plots in Figure 2b together

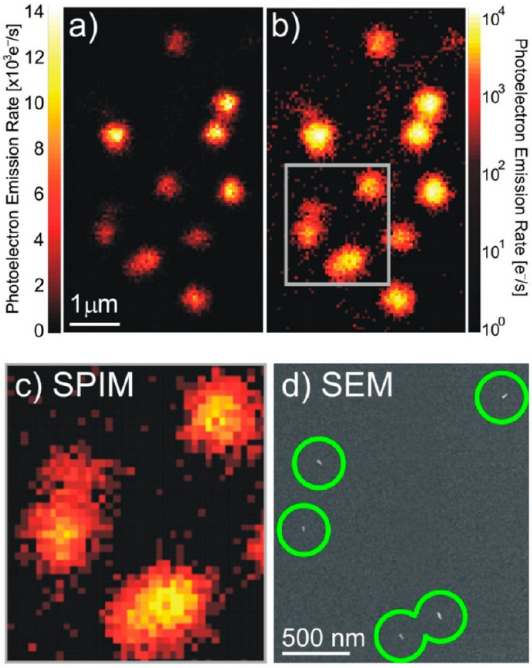

Figure 1. Multiphoton photoemission map of individual Au nanorods ($\langle L\rangle = 40(5)$ nm; $\langle W\rangle = 10(2)$ nm) on ITO plotted on a (a) linear and (b) logarithmic color scale. Images are recorded in a scanning photoionization microscope (SPIM) using circularly polarized ultrafast laser light ($\lambda = 800$ nm; $I = 6 \times 10^8$ W/cm^2; $\tau_P \approx 40$ fs). (c) SPIM and (d) SEM image of the same substrate area, indicated by a gray square in panel b, confirm that the observed photoemission signal originates from single Au nanorods on ITO.

with the best fit lines. For a sample of $N = 21$ rods, an average value of $\langle n\rangle = 3.2(2)$ is obtained; this implies a third order photoemission process, in good agreement with findings of previous studies under similar excitation conditions.[52,59] A comparison between SEM images of two representative nanorods (Figure 2c) and their corresponding polar plots of photoemissivity *versus* θ (Figure 2b) indicate that maximum photoemission occurs when the laser polarization angle (θ_0) aligns with the long rod axis (θ_{rod}). The 1:1 correspondence between θ_0 and θ_{rod} is demonstrated more quantitatively in Figure 2d for a sample of $N = 52$ nanorods, which reveals a straight line with the expected slope of ~1. Since the longitudinal plasmon resonance (along the Au nanorod long axis) is predominantly excited at $\lambda \approx$ 800 nm, these results confirm that enhanced photoelectron emission is observed for laser polarization spatially aligned with respect to the dipole moment of the resonant plasmon mode.

Plasmon Resonance. The central role plasmons play in multiphoton photoemission from metallic nanoparticles is further confirmed by the strong excitation wavelength dependence of the photoemission for individual Au nanorods. In the ultrafast excitation regime, pulse duration and spectral bandwidth are intimately related. Thus, to ensure the same temporal pulse width ($\tau_P \approx 40$ fs) at different center wavelengths (λ),

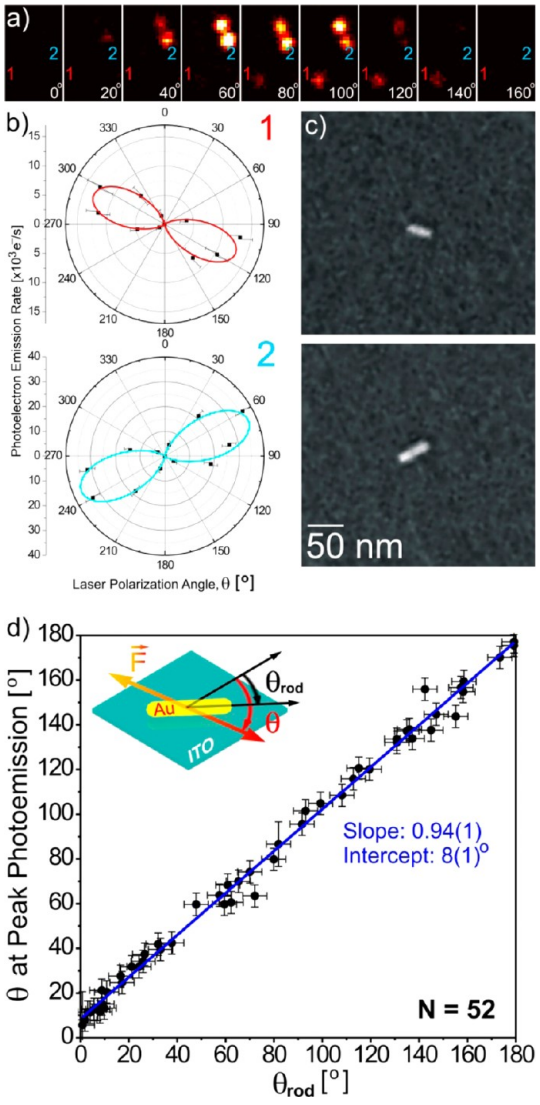

Figure 2. (a) Sequence of images of the same sample area recorded as a function of laser polarization angle θ, demonstrating a strong sensitivity in photoemission signal from Au nanorods. (b) Polar plots of photoemission rate *vs* θ and the corresponding SEM images for the two rods in panel a. Maximum photoelectron emission from a particular nanorod results when the laser polarization aligns with the rod long axis θ_{rod}. This observation is quantitatively confirmed in panel c, where the polarization angle resulting in maximum photoemission (θ_0) is plotted *vs* long axis orientation (θ_{rod}) for a sample of $N = 52$ nanorods.

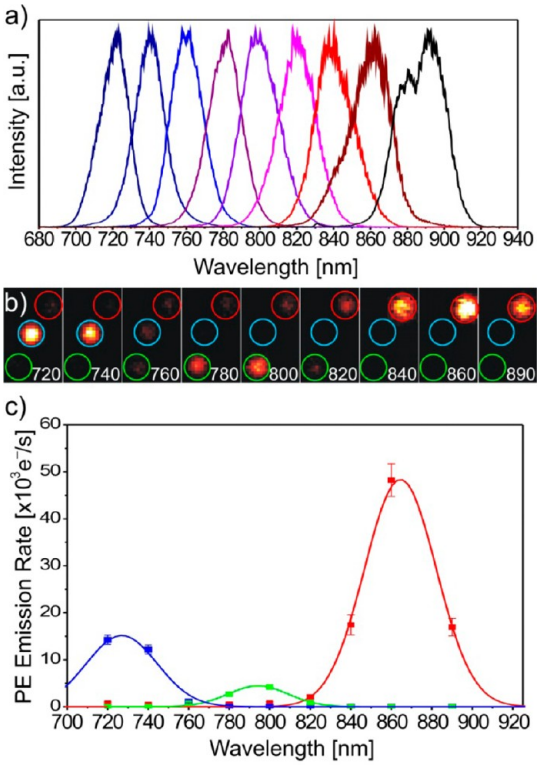

Figure 3. (a) Typical spectral profiles of the excitation laser as the center wavelengths is scanned across the available tuning range of the Ti:Sapphire oscillator (720−890 nm). (b) Sequence of SPIM images for fixed sample area recorded using circularly polarized excitation laser light of different center wavelengths. Photoelectron (PE) emission rates from individual nanorods depend sensitively on the center laser excitation wavelength, as shown in photoemission spectra (c) of the three rods identified in panel b.

the spectral width $\Delta\lambda$ must be correspondingly adjusted to satisfy the expression $\Delta\lambda = 0.44\lambda^2/(c\tau_P)$. The typical spectral profiles for pulses centered at various optical frequencies used for wavelength-dependent studies are qualitatively depicted in Figure 3a. In Figure 3b, a sequence of SPIM images is presented for a fixed sample area but as a function of laser excitation center wavelength. By plotting the photoemission rate from individual nanorods as a function of wavelength, we obtain photoemission spectra such as the ones shown in Figure 3c for the three rods identified in Figure 3b. The photoemission spectra clearly reveal optically resonant behavior, with photoemission signals from a particular nanorod decreasing by more than 2 orders of magnitude when excited more than 50 nm away from the plasmon resonance.

To unequivocally confirm that the observed photoemission resonances result from plasmonic excitation, corresponding dark-field scattering and photoelectron emission spectra need to be benchmarked for a significant sample of nanoparticles. Particle registration is a necessary prerequisite for achieving this goal, as demonstrated by SPIM and DFM images of the same sample region shown in Figure 4 panels a and b, respectively. The larger nanorods (Sample II) are used for these correspondence studies due to their greater (~16×) scattering cross sections compared with the smaller rods (Sample I). Lineouts through the signal obtained from the same nanorod are shown for both techniques in the bottom right corner of each subfigure. Note the vanishing ITO substrate background levels in the SPIM image; this corresponds to a typical signal-to-background (S/B) contrast ratio of 10^6, which should be compared to only about a 1.4:1 ratio for the DFM image. Furthermore, spatial resolution in these SPIM images ($w_3 \approx 290(10)$ nm) is additionally reduced

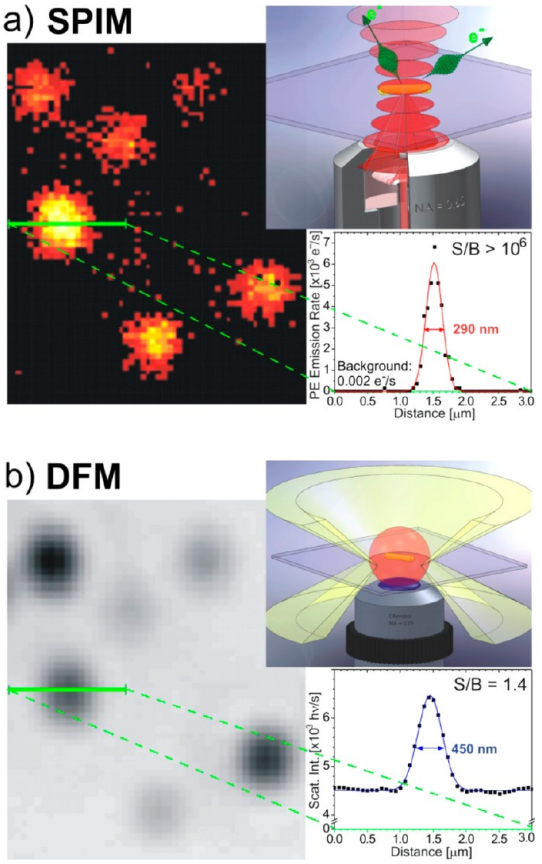

Figure 4. (a) SPIM and (b) DFM image of Au nanorods ($\langle L \rangle$ = 63(5) nm; $\langle W \rangle$ = 20(2) nm) in the same sample area, with a lineout from a single nanorod in each image (green line) plotted in the lower right corner. Background-free nature and subdiffraction limited resolution of the SPIM technique is apparent. Conceptual depictions of the SPIM and DFM setups are shown in the top right corner of each subplot.

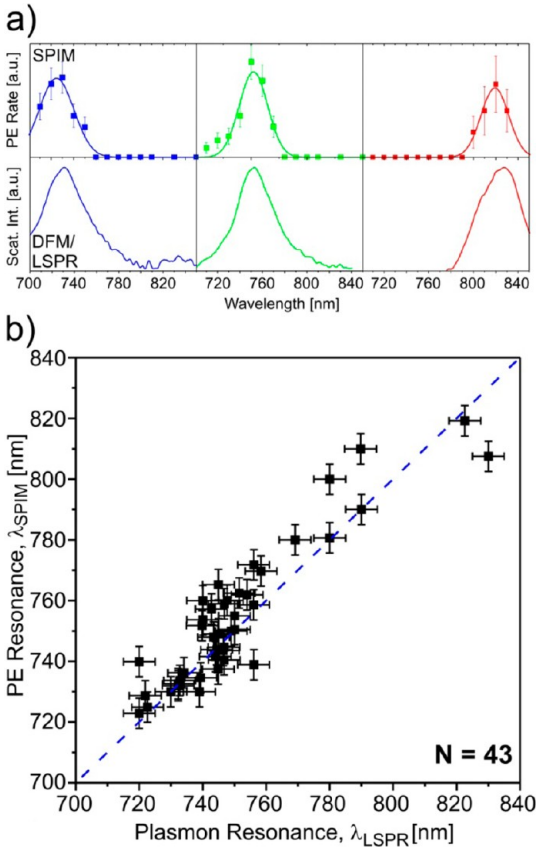

Figure 5. (a) Photoemission (top) and corresponding scattering (bottom) spectra of three representative Au nanorods ($\langle W \rangle$ = 20(2) nm), measured in SPIM and DFM, respectively. Correspondence between the multiphoton photoemission resonances λ_{SPIM} and the plasmon resonances λ_{LSPR} is apparent. (b) λ_{SPIM} as a function of λ_{LSPR} for N = 43 nanorods, where a dashed line designates the theoretically predicted 1:1 correspondence between λ_{SPIM} and λ_{LSPR}.

compared with respect to 1-photon scattering signal in DFM images ($w_1 \approx 450(5)$ nm), due to the multiphoton nature of the photoemission process. Once again, the observed resolution improvement is in good agreement with $w_n \approx w_1/\sqrt{n} = 260(3)$ nm, where the order of the photoemission process for Au rods on ITO is $n = 3$.

Representative photoemission spectra (SPIM) together with the corresponding Au nanorod scattering spectra (DFM) are shown in Figure 5a. In all cases, peak photoemission results at wavelengths where the localized surface plasmon resonance (LSPR) is observed in the scattering spectra. This behavior is further quantified for $N = 43$ studied rods in Figure 5b, where a one-to-one correspondence is clearly observed (dashed line) between photoemission resonances, λ_{SPIM}, and localized surface plasmon resonances, λ_{LSPR}. The results unambiguously illustrate the rigorous link between peak multiphoton photoemission and resonant excitation of the nanoparticle plasmon mode.

By way of additional confirmation, we have explored the correlation between (i) photoemission spectral properties and (ii) Au nanorod *structure*. We focus specifically on aspect ratio (AR) as the dominant structural factor influencing the longitudinal LSPR energies, with larger AR values leading to increasingly more red-shifted longitudinal plasmon resonances. This expectation is confirmed in Figure 6, where photoemission spectra are shown alongside the SEM images of two representative Au nanorods. Specifically, the rod with larger AR exhibits a clearly red-shifted peak in photoemission, consistent with an equivalent red-shift in the longitudinal plasmon resonance.

Plasmon Resonance Width. In addition to resonance *frequencies*, resonance *widths* of the plasmonic nanoparticles are also of interest and contain complementary information on the plasmon lifetime. In the small-particle limit, the measured resonance width ($\Delta\nu_{Plasmon}$) arises from three contributions: $\Delta\nu_{bulk}$ is due to bulk electron–phonon and electron–electron scattering, $\Delta\nu_{surf}$ originates from electron–surface scattering, and $\Delta\nu_{rad}$ comes from radiation damping. While the first term is material-specific ($\Delta\nu_{bulk} \approx 75$ meV for Au in 1–2 eV range),[72] the latter terms do depend sensitively on particle size and shape. For rods with typical dimensions encountered in this work, previous single-particle studies have reported

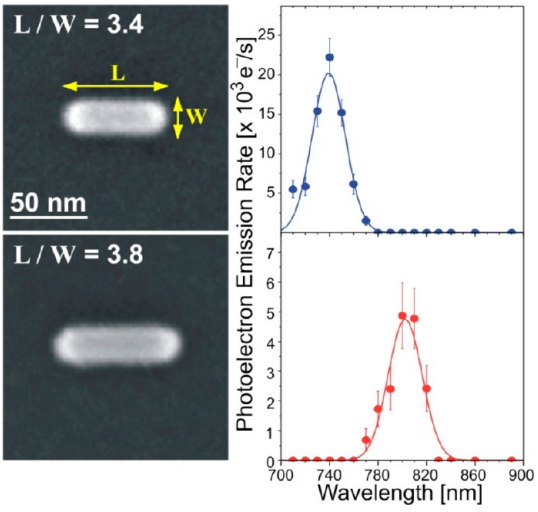

Figure 6. SEM images (left) and the corresponding photoemission spectra (right) of two Au nanorods with different aspect ratios (AR = *L*/*W* = length/width). As expected, an increased rod aspect ratio results in a red-shifted longitudinal LSP resonance.

$\Delta\nu_{Plasmon} \approx 110$ meV.[78] This is in good agreement with the mean value of $\langle\Delta\nu_{Plasmon}\rangle = 106(1)$ meV measured in the present work (Sample II, $N = 140$ rods), indicating a plasmon lifetime on the order of $\tau_{PI} \approx 6$ fs.

It is less clear what dictates the SPIM photoemission resonance widths and what information may be inferred for dynamics of the excited electrons. To explore this issue, we compare natural linewidths of longitudinal plasmon modes $\Delta\nu_{Plasmon}$, measured in DFM, with photoemission resonance widths $\Delta\nu_{SPIM}$, measured in SPIM, for a series of Au nanorods. For example, photoemission and dark-field scattering resonances for a representative Au rod are shown in Figure 7a. To extract the natural linewidth of the multiphoton photoemission resonance, the spectral width of the ultrafast probe laser (46 meV) is deconvolved from the measured spectrum to reveal the underlying resonance profile (red line). Interestingly, this photoemission resonance width, $\Delta\nu_{SPIM} = 50(5)$ meV, is signficantly *smaller than* the natural plasmon width, $\Delta\nu_{Plasmon} = 92(2)$ meV. In fact, the photoemission resonances are generally ~2-fold narrower than the corresponding scattering resonances, as shown in Figure 7b for a sample of $N = 18$ rods. Specifically, a dashed trendline with $\Delta\nu_{SPIM} = \Delta\nu_{Plasmon}/2$ captures the observed behavior quite well in 15 out of 18 rods (*i.e.*, 83%), with the remaining three (*i.e.*, 17%) exhibiting substantially broader photoemission resonances. We will address the reasons for such a trend in the section below.

DISCUSSION

The correlation in Figure 5b between (i) SPIM *photoemission* and (ii) dark-field *optical* resonances in Au nanorods clearly underscores the critical role of plasmons in multiphoton photoelectron emission from metallic nanoparticles. This is further corroborated by

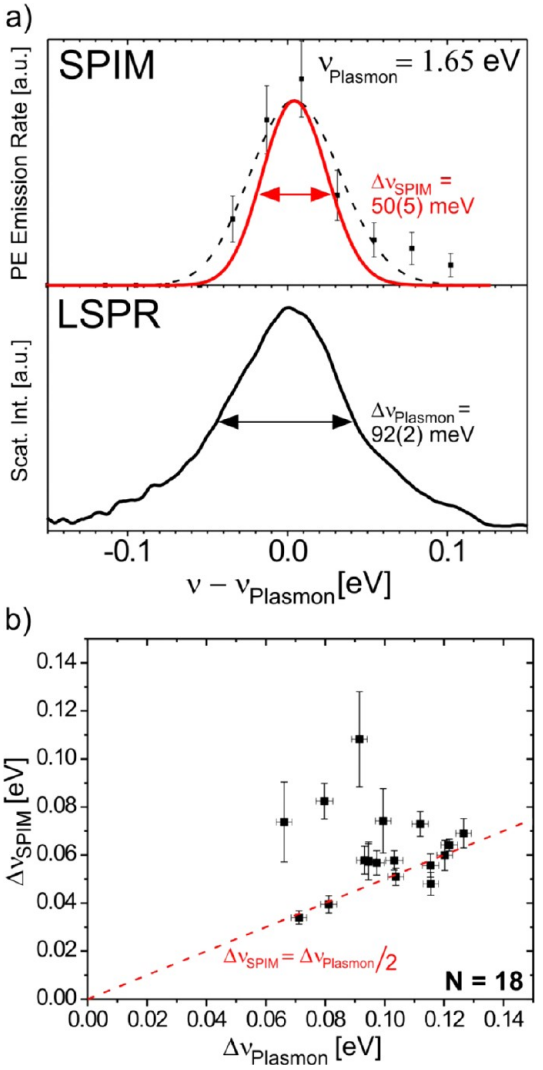

Figure 7. (a) Photoemission (top) and scattering (bottom) spectra of a representative, isolated Au nanorod (<W> = 20(2) nm) centered at the longitudinal plasmon resonance ($\nu_{Plasmon}$ = 1.65 eV). Gaussian nonlinear least-squares fit to the experimental data points before (black dashed line) and after (solid red line) deconvolution of the excitation laser spectral width (ΔE = 0.046 eV) are indicated. Linewidth narrowing is observed in SPIM ($\Delta\nu_{SPIM}$) *vs* DFM ($\Delta\nu_{Plasmon}$), consistent with the $n = 3$ multiphoton nature of the SPIM signal. (b) $\Delta\nu_{SPIM}$ as a function of plasmon natural line width, $\Delta\nu_{Plasmon}$, for a sample of $N = 18$ Au nanorods. Dashed red line marks the expected trend for coherent three-photon photoelectron emission (see text for details).

observation that maximum multiphoton photoemission occurs when the laser polarization aligns with the direction of the longitudinal plasmon mode (see Figure 2b), as also observed previously for epitaxially grown nanostructures.[59] To better understand how the plasmon mediates multiphoton photoemission from metallic nanoparticles, we compare our experimental observations with theoretical predictions from a coherent multiphoton photoelectron emission model recently proposed by Yalunin *et al.*[74] While a number of descriptions exist for coherent multiphoton photoelectron emission from *planar, free-electron* metal surfaces,[79−83] we focus

on the aforementioned model for two reasons. First of all, it accounts for both the high frequency/low intensity (*i.e.*, multiphoton photoelectric effect) as well as low frequency/high intensity (*i.e.*, optical field emission) limits of the same underlying electric-field induced electron emission mechanism, with a relatively smooth transition between the two regimes. Second, although the model was developed for continuous laser field excitation, it accurately describes photoemission for pulsed light sources as well, provided that the excitation pulse contains at least ~10 cycles (*i.e.*, $\tau_P > 25$ fs for 800 nm).

To empirically include the effect of the localized surface plasmon (LSP), we simply scale the incident E_0 by the near-field enhancement factor $|\eta_{ENH}^{MAX}|$ and use the resulting total electric field $E = E_0 \times |\eta_{ENH}^{MAX}|$ in the calculations. Such a classical treatment is justified due to a much larger number of plasmons ($N_{pl} \approx (3 \times 10^{-10}$ cm$^2) \times (2 \times 10^{13}$ ph/cm^2/pulse) = 6000) generated per laser pulse under our experimental conditions compared to the much smaller number ($N_{pl} = 3$) annihilated upon photoelectron emission. All other assumptions inherent to the original model are preserved, thus neglecting electron-surface scattering and other effects that may need to be considered due to finite nanoparticle size. To independently obtain $|\eta_{ENH}^{MAX}|$ values, we numerically calculate the particle near-field enhancements (and far-field properties) in COMSOL software for a representative Au rod (L = 80 nm; W = 20 nm) in vacuum. Such a representative near-field distribution surrounding the rod at the longitudinal plasmon resonance is shown in Figure 8a with a large E field enhancement clearly observable at the nanorod tips. More quantitatively, a lineout along the major axis (Figure 8b) reveals significantly enhanced local electric fields with $|\eta_{ENH}^{MAX}| \approx 60$.

Since the photoemission rate N_{PE} depends sensitively on the magnitude of the incident electric field $|E|$ in coherent MPPE models, scaling approximately as $|E|^{2n}$, where n is the order of the photoemission process, such sizable electric field enhancement factors can have an extremely large effect on the photoemission yield. For example, in case of unenhanced electric fields (*i.e.*, $E = E_0$), predicted photoelectron intensities are approximately 10^{10} fold *lower* than experimentally measured. Conversely, due to the exceptionally rapid power dependence on $|E|$,[6] inclusion of electric near-field enhancement ($|\eta_{ENH}^{MAX}| \cong 60$ at rod tips) in the calculations generates a potential additional factor of $60^6 \approx 4 \times 10^{10}$, which nicely makes up for the low initial photoemission predictions. Indeed, this simple model now even *overestimates* the observed photoemission rate by approximately an order of magnitude (see Figure 9a). However, as $|\eta_{ENH}|$ decays with distance from the nanorod, the predicted photoemission rates should be taken as upper limit estimates in excellent semiquantitative agreement with the experimental results. In these calculations, the emitter area is assumed to be the surface

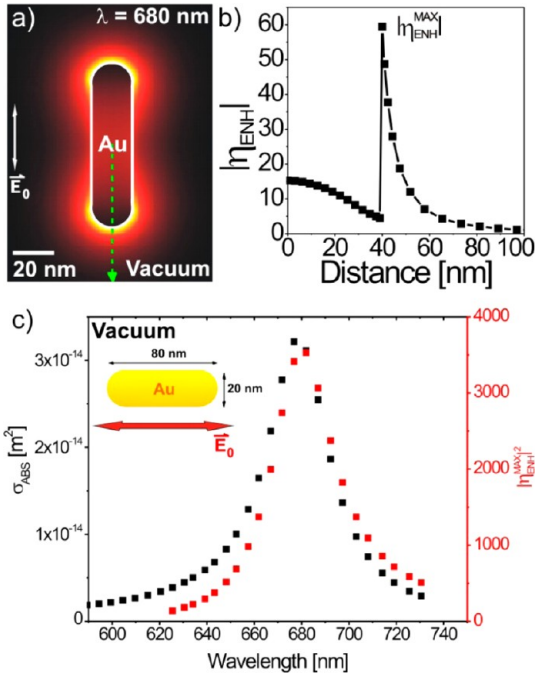

Figure 8. (a) The electric near-field enhancement upon resonant excitation of the longitudinal plasmon resonance (λ = 680 nm) for a Au nanorod (L = 80 nm × W = 20 nm) in vacuum. (b) Enhancement factor $|\eta_{ENH}|$ as a function of distance along the rod long axis, with a maximum value of $|\eta_{ENH}^{MAX}| = 60$ observed at the rod tip and decreasing to 1/e at a distance $d \approx W/2$ from the rod surface. (c) Calculated $|\eta_{ENH}^{MAX}|^2$ and σ_{ABS}, revealing a nearly identical dependence on laser excitation wavelength.

of the rod tips, which exhibit strongest electric field enhancements (see Figure 8a). Of special importance, the $|E|^6$ (*i.e.*, I^3) dependence of the photoemission rates is reproduced quantitatively, signaling that a coherent, multiphoton photoelectric effect is indeed responsible for the experimentally observed photoemission rates.

To model the laser polarization dependence of the photoemission current, the near-field enhancement factor is further modified with the following expression:

$$|\eta_{ENH}^{MAX}|(\theta) = |\eta_{ENH}^{MAX}|_0 \cos(\theta - \theta_0) \quad (1)$$

where θ is the laser polarization angle, θ_0 is the rod long axis orientation, and $|\eta_{ENH}^{MAX}|_0 \approx 60$ is the maximum near-field enhancement factor value. The predicted behavior is plotted in Figure 9b and is well described by $N_{PE} \propto \cos^{2n}(\theta - \theta_0)$, where n is the order of the photoemission process and is in quantitative agreement with experimental observations.

Similarly, the enhancement factor $|\eta_{ENH}^{MAX}|^2$ can be modified based on a presumed Lorentzian line shape (see Figure 8c) to model the photoelectron emission rate as a function of optical laser frequency:

$$|\eta_{ENH}^{MAX}|^2(\nu) = |\eta_{ENH}^{MAX}|_0^2 \frac{\Delta\nu_{Plasmon}^2}{4(\nu - \nu_{Plasmon})^2 + \Delta\nu_{Plasmon}^2} \quad (2)$$

where $|\eta_{ENH}^{MAX}|_0$ is the peak electric field enhancement factor at the resonant frequency $\nu_{Plasmon}$. The resonance

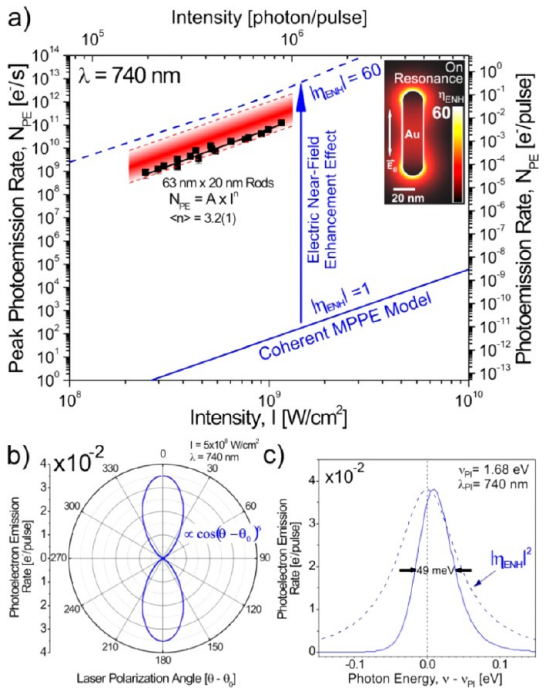

Figure 9. (a) Photoemission rate *vs* laser intensity (λ = 740 nm) for polarization parallel to the rod long axis: (black squares) experimental data for a resonantly excited representative Au nanorod in Sample II ($\lambda_{Plasmon} \approx 740$ nm); (black line) nonlinear least-squares fit to the experimental data; (red shaded area) range of experimentally observed photoemission rates for different rods in the Sample; (blue line) coherent multiphoton photoelectron emission model (MPPE) from reference 74 in the absence (solid) and presence (dashed) of typical electric near-field enhancements $|\eta_{ENH}^{MAX}|$ = 60 encountered near the rod tips on plasmon resonance (see the near-field map in the inset). Note that the peak photoemission rates (left *y* axis) should be multiplied with the duty cycle $\tau_P \times \nu_{rep} = 5 \times 10^{-6}$ to yield experimentally measured rate values. (b) Predicted, near-field enhanced, coherent multiphoton photoemission rate at λ = 740 nm as a function of the laser polarization angle θ relative to the rod long axis orientation θ_0. (c) Analogously calculated photoemission rate as a function of the photon energy with respect to the longitudinal plasmon resonance, $\lambda_{PI} = 740$ nm (ν_{PI} = 1.68 eV, $\Delta\nu_{PI}$ = 0.10 meV). The following typical experimental conditions are employed in the calculations: laser intensity $I = 5 \times 10^8$ W/cm^2, pulse duration τ_P = 50 fs, near-field enhancement factor $|\eta_{ENH}^{MAX}| = 60$.

width $\Delta\nu_{Plasmon} \approx 100$ meV is chosen to conform to typical experimental values for Au nanorods, as in Figure 7. The calculated photoemission spectrum, shown as a dashed line in Figure 9c, captures the experimentally observed behavior, with peak photoemission nicely coinciding with the longitudinal plasmon resonance (see Figure 5). Interestingly, the theoretically predicted photoemission resonance line shape exhibits a fwhm approximately one-half of the plasmon resonance width (*i.e.*, $\Delta\nu_{SPIM} \approx \Delta\nu_{Plasmon}/2$), also consistent with the data in Figure 7.

It is worth noting that these calculations predict photoemission peaks to be slightly *blue*-shifted ($\Delta\nu \approx +9$ meV) compared to the frequency of the electric near-field enhancement maximum. This is a consequence of the increased share of conduction electrons that can be promoted to the vacuum level by the more energetic photons, thus resulting in peak-pulling of photoemission resonances toward the blue end of the spectrum. This effect counteracts the well-known red-shift of the absorption/scattering resonances relative to the electric near-field enhancement maxima due to plasmon damping.[68−71] The magnitude of the *red*-shift $\Delta\nu \approx -8$ meV, inferred from data in Figure 7c, indicates that the two effects effectively cancel in the case of the longitudinal LSP. This in turn results in nearly coincident photoemission and scattering resonances for Au nanorods, in excellent agreement with experimental observations.

Since excitation conditions resulting in efficient multiphoton photoemission from Au nanorods also lead to strongly enhanced light absorption by the particles (see Figure 7c), it is important to consider possible thermal contributions to photoemissivity due to particle heating. For example, the incident laser may transiently heat the metal to very high temperatures, raising a fraction of conduction electrons to the vacuum level, where electron emission becomes possible. Such thermionic emission, generally described by the Richardson−Dushman equation,[84−86] turns out to be relevant only for electron temperatures exceeding several thousand degrees Kelvin. Under our most intense experimental conditions (τ_P = 50 fs, $I = 10^9$ W/cm^2), a back-of-the-envelope calculation for a typical Au nanorod (L = 60 nm × W = 20 nm) with a calculated $\sigma_{ABS} = 3 \times 10^{-10}$ cm^2 yields a maximum temperature rise of $\Delta T_{MAX} \approx 400$ K with essentially complete cooling between laser pulses. At $T_{MAX} \approx 700$ K, any contributions due to transient heating and resulting thermionic emission from the bulk can be safely neglected.

While such temperatures suggest a negligible role for bulk thermionic emission, it is important to also consider the effect of femtosecond laser radiation on *electronic* temperature. It is well-known that upon ultrafast excitation the conduction electrons in a metal thermalize within a few hundred femtoseconds ($\tau_{e\text{-}therm}$ = 200−500 fs),[87] but remain uncoupled from the lattice, due to the relatively slow electron−lattice thermalization (*ca.* 1−10 ps).[88] Combined with their order of magnitude lower specific heat capacities, this results in an electron gas momentarily becoming significantly hotter than the bulk, leading to a phenomenon called "anomalous heating". As a rough estimate of this electron temperature jump T_{max}^e, we consider the Sommerfeld model for which the heat capacity of conduction electrons in metals increases linearly with temperature. Separation of variables yields a simple differential equation for the temperature rise, which when integrated with all cooling to the lattice and/or substrate neglected yields

$$T_{max}^e = \sqrt{T_0^2 + \frac{2\sigma_{ABS} I \tau_P T_F}{\pi^2 N_e V_{NP} k_B}} \qquad (3)$$

where N_e is conduction electron density (for Au, 5.9 × 10^{22} cm^{-3}), T_F is the Fermi temperature (for Au, 6.4 × 10^4 K), V_{NP} is the nanorod volume, k_B is the Boltzmann constant, T_0 is the initial temperature (298 K), and all other quantities as defined previously. At the highest employed laser intensity $I = 10^9$ W/cm^2, eq 3 predicts $T^e_{max} \approx 4000$ K, implying sufficiently high transient electronic temperatures to promote contributions from anomalous thermionic emission. However, the rate of such a thermally activated process is predicted to depend exponentially on laser intensity, which differs quite fundamentally from the experimentally observed power law dependence more consistent with the coherent multiphoton model predictions (see Figure 9a). Thus, we can safely rule out anomalous thermionic emission as a significant contributor to the measured photoemission current even under the most intense laser excitation conditions.

With experimental evidence strongly underscoring the role of plasmon-induced electric near-field enhancement in mediating electron emission, it is interesting to consider some alternative E-field driven electron emission mechanisms as well. In particular, the large near-field enhancement factors for plasmonic nanoparticles lead to an intriguing possibility of optical field emission (OFE), whereby strong electric fields facilitate tunneling of conduction through the work function barrier into vacuum. To determine whether the excitation conditions favor a multiphoton photoelectric effect (perturbative regime) or optical field emission (nonperturbative regime), the so-called Keldysh parameter is generally employed:[79]

$$\gamma = \sqrt{\frac{2m_e\omega^2\Phi}{e_0^2E^2}} \quad (4)$$

where m_e (e_0) is the electron mass (charge), ω is the angular frequency of light, E the electric field amplitude and Φ is the material work function. For $\gamma < 1$, the tunneling mechanism is more applicable, whereas for $\gamma > 1$, electron emission is dominated by coherent multiphoton photoelectron emission. At our typical electric field intensities of $E = 0.1$ V/nm ($I \approx 10^9$ W/cm^2), near-field enhancement factor $|\eta^{MAX}_{ENH}|_0 \approx 60$, and frequencies $\omega = 2.5 \times 10^{15}$ s^{-1} ($\lambda = 740$ nm), yields $\gamma \approx 3$, suggesting borderline operation in the mulitphoton photoelectric regime. This conclusion is further supported by the clear power law intensity dependence of the photoemission current, which would be exponential if the tunneling mechanism were dominant.

However, the mere implication that plasmon-resonant ultrafast excitation of supported Au nanorods may result in optical field emission at relatively modest laser intensities ($I \approx 10^{10}$ W/cm^2) is quite remarkable, especially in light of 10^2 fold higher intensities typically required in traditional optical field emitters, such as metallic tips.[45,46] While it remains to be determined whether rods can withstand a 10-fold increase in incident laser intensity without melting, first hints of an impending transition point ($\gamma \approx 1$) may be observable at the present intensity levels already. Near the transition, some electrons may absorb more than the minimum number of photons required for ionization (*i.e.*, $n > 3$ in the present case), thus resulting in above-threshold ionization, where electrons of relatively high kinetic energy (*i.e.*, KE > 5 eV) can be emitted. In studies of electron emission from roughened metal surfaces and nanoparticles, even more highly energetic electrons (KE ≈ 0.5 keV) have been observed due to ponderomotive acceleration of emitted charges in the plasmonically enhanced local electric field.[55,89−91] Energy-analysis of the emitted electrons from Au nanorods and observation of high KE electrons could thus provide clear evidence for a transition point into the optical field emission regime. Toward this end, we are currently adding velocity map imaging (VMI) capability to our existing experimental setup, which will not only provide information on the KE of photoemitted electrons, but also on their angular distribution.

SUMMARY

Multiphoton photoelectron emission from individual, supported Au nanorods on ITO was studied following excitation with ultrafast laser pulses ($\tau_P \approx$ 50 fs) in the longitudinal plasmon resonance spectral region near 700−900 nm. Photoemission rates are found to depend strongly on the laser polarization, specifically peaking when the laser polarization aligns with the longitudinal plasmon mode (*i.e.*, rod long axis). As a function of excitation laser wavelength, (i) three-photon photoemission rates and (ii) one-photon optical scattering are shown to peak at the same resonance frequencies. Both findings identify the critical role of plasmons in mediating multiphoton photoelectron emission from metallic nanoparticles and quite likely nanoscopically rough surfaces as well. The dramatic increase in photoemission yield can be thought to arise from the plasmon enhancing the incident electromagnetic field in the particle near-field, thus facilitating conduction electrons to overcome the material work function and be emitted. In the MPPE regime, the near-field enhancement is more properly considered part of the multiphoton photoemission cross-section instead of the excitation conditions (*i.e.*, electric field amplitude), thereby manifesting itself in the increased rate of the multiphoton process. This simple physical picture is corroborated by agreement between the experiment and theory proposed by Yalunin *et al.* for coherent (direct) multiphoton photoemission,[74] modified simply by use of an *enhanced* near-electric field predicted from numerical COMSOL calculations. These results again support coherent multiphoton photoemission as the predominant mechanism for photoelectron emission from metallic nanoparticles upon femtosecond

($\tau_p \approx 50$ fs), medium-intensity ($<10^{10}$ W/cm^2) excitation near the surface plasmon resonance. According to the model, *n*-photon photoelectron emission rate should scale as the near-field enhancement factor $|\eta_{ENH}|^{2n}$. Thus, for typical values encountered near rod tips (*i.e.*, $|\eta_{ENH}| = 60$), such three-photon photoelectron emission rates are predicted to be $\sim 10^{10}$ stronger than in the absence of any plasmonic near-field enhancement. This dramatic sensitivity to local electric fields showcases the potential for such photoemission-based SPIM imaging methods to complement optical techniques and thereby offer additional insight into the near-field properties of plasmonic nanostructures/nanoparticles.

MATERIALS AND METHODS

Sample Preparation. Commercially available aqeuous solutions of two samples of bare Au nanorods (Nanorodz; Nanopartz, Inc.) are used for the present studies: (Sample I) Smaller gold nanorods with nominally 45 nm (length, *L*) × 10 nm (width, *W*) dimension (Nanopartz P/N: 30-10-850) and (Sample II) larger ones with specified dimensions 86 nm (*L*) × 25 nm (*W*) (Nanopartz P/N: 30-25-750). Dimensional analysis using SEM and TEM on the obtained samples yields the following, actual ensemble-averaged values for rod dimensions and aspect ratios (AR) with standard deviation reported in parentheses: (i) Sample I ($N = 72$): $\langle L \rangle = 40(5)$ nm, $\langle W \rangle = 10(2)$ nm, $\langle AR \rangle = 3.9(6)$. (ii) Sample II ($N = 385$): $\langle L \rangle = 63(5)$ nm, $\langle W \rangle = 20(2)$ nm, $\langle AR \rangle = 3.2(3)$. In both solutions, cetyl-trimethyl-ammonium-bromide (CTAB) is added by the supplier to stabilize the colloidal solution. The UV−vis spectrum of the stock aqeuous solution of the smaller Au nanorods (Sample I) exhibits a strong peak due to the longitudinal plasmon resonance at $\langle \lambda_{Pl} \rangle_L = 820(2)$ nm with a 1σ width, $\sigma_L = 60$ nm, and a weaker one due to the transverse plasmon resonance at $\langle \lambda_{Pl} \rangle_T = 510(1)$ nm and a width $\sigma_T = 13$ nm. For the sample of larger Au nanorods (Sample II) the peaks are observed at $\langle \lambda_{Pl} \rangle_L = 725(2)$ nm and $\langle \lambda_{Pl} \rangle_T = 512(1)$ nm with the corresponding 1σ widths $\sigma_L = 35$ nm and $\sigma_T = 14$ nm, respectively. Unless noted otherwise, the values in parentheses throughout this paper report the standard error of the mean.

The nanoparticles are deposited on a standard glass coverslip (Corning 1 ½) coated with a thin, nominally 10 nm thick, indium−tin oxide (ITO) layer (Thin Film Devices, Inc.) by spin-casting 40 μL of aqueous stock solution of Au nanorods onto a rotating (1500 rpm) coverslip until solvent evaporates (5 min). The sample is then sequentially rinsed with deionized water, methanol, and acetone to remove any noncolloidal solute (*i.e.*, cetyl-trimethyl-ammonium bromide (CTAB)). To allow particle registration, a Au pattern from an indexed TEM grid template is deposited on the coverslip before the sample is spin-cast. The slides are prepared by first vapor-depositing a 70 nm Au film on ITO slides, which have been previously cleaned in an oxygen plasma source and rinsed with methanol. Positive photoresist (Shipley; Microposit S1813) is spin-cast at 3000 rpm on top of the Au film. The slide is then heated for 2 min on a hot plate maintained at 115 °C. An uncoated indexed TEM grid (Electron Microscopy Sciences; LF400-Cu) is used as a mask during 10 s exposure to 436 nm line from a mercury lamp for a total dose of 150 mJ/cm^2. The irradiated photoresist is removed by a 30 s dip in a developer solution (Shipley; Microposit MF CD-26) to expose the underlying Au layer. A 60 s dip in etchant solution (Transene, Inc.; Gold Etch Type TFA) removes the Au film from those areas, leaving a "positive" image of the initial mask on the ITO. The coverslip is thoroughly rinsed with acetone and methanol to remove the remaining photoresist and is, prior to use, exposed to ozone for 15 min to remove any built-up hydrocarbons.

Scanning Photoionization Microscopy. Tunable fundamental output ($\lambda = 720-890$ nm; $E_{h\nu} = 1.72-1.39$ eV) of a high-repetition rate ($\nu_{rep} = 90$ MHz), ultrafast Ti:Sapphire laser system is guided into a vacuum chamber maintained at $\sim 5 \times 10^{-7}$ Torr, where a reflective-type microscope objective (Numerical Aperture, NA = 0.65) focuses the beam to a diffraction limited spot on the sample. High laser intensity at the focus promotes a fraction of the electrons within the probed material to the vacuum level, where they are detected by a channeltron electron multiplier located ~1 cm above the sample. At typical material work functions ($\Phi_{Au} = 4.6-5.1$ eV,[92] $\Phi_{ITO} = 4.4-4.7$ eV depending on the crystal facet[93]), $n = 3-4$ photons with λ in the 700−900 nm range ($n > \Phi/E_{h\nu}$) are energetically required to emit a single photoelectron. The region of interest is raster scanned *in vacuo* by applying voltages to the three piezoelectric cylinders that kinematically support the sample stage. For a more detailed description of the technique, the reader is referred to previously published work.[51,94]

Dark-Field Microscopy. A commercial inverted microscope (Olympus IX-71) with a dark-field illuminator operating in transmission mode is employed. Unpolarized, white light from a tungsten/halogen lightsource is focused onto the sample coverslip by a dry dark-field condenser (Olympus U-DCD, NA = 0.80−0.92). Scattered light is collected by a 40× Plan Fluorite infinity-corrected air objective (Olympus UPLFLN40X, NA = 0.75) and sent to a side-port where the wide-field image is first magnified 3.4× by an achromatic lens pair ($f_1 = 200$ mm, $f_2 = 60$ mm) and finally focused by an achromatic lens ($f_3 = 200$ mm) onto the front slits of the spectrometer (Acton SpectraPro 150, 150 grooves/mm diffraction grating). The diffracted light (1st order) from individual nanoparticles is 1:1 imaged onto an EMCCD camera (Princeton Instruments, Cascade II), which is in present studies operated without multiplication. When imaged directly (diffraction grating set to zeroth order) the nanorods appear as diffraction-limited Airy discs of size $d_{Airy}^{CCD} = 9.5$ px × 16 μm/px = 152 μm. Given the total system magnification (134×) the apparent spot size, $d_{Airy} = 1130$ nm is in good agreement with the expected diffraction-limited value ($d_{DL} = 1.21 \times \lambda/NA = 1210$ nm for $\lambda = 750$ nm). To ensure complete integration of the scattered light collected from a particular scatterer and minimize the noise contributions to the integrated signal, ~20 px wide horizontal strips at particle positions are hardware binned to acquire the single-particle scattering spectra. To reduce background, the signal is subtracted for a horizontal strip of identical thickness in a region without nanoparticles. To correct for spectral nonuniformity, the background-subtracted signals are scaled by lightsource spectral response. The spectrum of the lightsource itself is collected by scattering from a bare coverslip under slightly out-of-focus dark-field illumination conditions, with all other settings identical to those employed during collection of the single-particle spectra.

Scattering spectra of Au nanorods are recorded immediately after preparing the samples as well as following the SPIM studies. No differences between spectra obtained before and after SPIM are observed, suggesting that at typical SPIM conditions little to no damage due to heating or potentially electron-induced chemical modifications occurs. Owing to prohibitively low scattering intensities from the smaller Au rods (Sample I), dark-field scattering studies are only feasbile and therefore performed on the larger Au rods (Sample II).

Secondary Electron Microscopy. All SEM images are acquired on FEI Nova NanoSEM 630 system with the through-lens detector (TLD) in immersion mode. The front grid of the detector is biased to ~ +150 V to improve collection of secondary electrons. With 10 kV electrons, 1.5 spot size, and 90 μs integration times, a signal-to-noise ratio S/N ≈ 20 and spatial resolution of *ca.* 1−2 nm are routinely achieved. In all correlated SPIM/DFM/SEM studies, the SEM characterization of the Au nanorod samples is performed last, due to the known degradative effect of electron microscopies.[95]

Theoretical Methods. The near-field distribution of electric fields as well as far-field properties (*i.e.*, absorption, scattering,

and extinction spectra) of Au nanorods are numerically calculated with a finite element method (FEM) implemented in COMSOL (v4.2). The plasmonic response of the nanoparticle depends rather sensitively on the exact particle shape, with significant distinctions in the far-field properties noted between, say, ellipsoidal *versus* lozenge structures.[96,97] Hence, in agreement with characteristic SEM shape distributions observed for chemically synthesized Au nanoparticles, the nanorods in the current study are most appropriately modeled as hemispherically capped cylinders (*i.e.*, lozenges), with bulk dielectric properties for Au as previously reported in the literature.[98]

The coherent multiphoton photoemission predictions are based on the proposed model by Yalunin *et al*. with all implemented adjustments described in the Discussion section.[74] In place of material specific parameters in the model, the following material properties of Au are used: metal work function Φ_{Au} = 4.8 eV (average of reported values 4.6−5.1 eV),[92] Fermi energy E_F = 5.5 eV. For estimates of particle temperature rise, the gold specific heat capacity c_{Au} = 0.129 J/g·K and density ρ_{Au} = 19.3 g/cm^3 are employed. Nanoparticle volume is calculated based on the lozenge model for the rod $V_{NP} = (\pi W^2/4)(L - W/3)$, where L and W are rod length and width, respectively.

Conflict of Interest: The authors declare no competing financial interest.

Acknowledgment. This work has been supported by the Air Force Office of Scientific Research (FA9550-12-1-0139), with additional funds for optics, microscopy and computer resources provided by the National Science Foundation (CHE1012685, PHYS1125844) and the National Institute for Standards and Technology. We also gratefully acknowledge D. Alchenberger for help with the SEM instrumentation and the ellipsometry.

REFERENCES AND NOTES

1. Mie, G. Articles on the Optical Characteristics of Turbid Tubes, Especially Colloidal Metal Solutions. *Ann. Phys., Berlin* **1908**, *25*, 377–445.
2. El-Sayed, M. A. Some Interesting Properties of Metals Confined in Time and Nanometer Space of Different Shapes. *Acc. Chem. Res.* **2001**, *34*, 257–264.
3. Kelly, K. L.; Coronado, E.; Zhao, L. L.; Schatz, G. C. The Optical Properties of Metal Nanoparticles: The Influence of Size, Shape, and Dielectric Environment. *J. Phys. Chem. B* **2003**, *107*, 668–677.
4. Kreibig, U.; Vollmer, M. *Optical Properties of Metal Clusters*; Springer-Verlag: Heidelberg, Germany, 1995; Vol. 25, p 532.
5. Sosa, I. O.; Noguez, C.; Barrera, R. G. Optical Properties of Metal Nanoparticles with Arbitrary Shapes. *J. Phys. Chem. B* **2003**, *107*, 6269–6275.
6. Frens, G. Controlled Nucleation for Regulation of Particle-Size in Monodisperse Gold Suspensions. *Nature* **1973**, *241*, 20–22.
7. Jin, R. C.; Cao, Y. W.; Mirkin, C. A.; Kelly, K. L.; Schatz, G. C.; Zheng, J. G. Photoinduced Conversion of Silver Nanospheres to Nanoprisms. *Science* **2001**, *294*, 1901–1903.
8. Nikoobakht, B.; El-Sayed, M. A. Preparation and Growth Mechanism of Gold Nanorods (NRs) Using Seed-Mediated Growth Method. *Chem. Mater.* **2003**, *15*, 1957–1962.
9. Oldenburg, S. J.; Averitt, R. D.; Westcott, S. L.; Halas, N. J. Nanoengineering of Optical Resonances. *Chem. Phys. Lett.* **1998**, *288*, 243–247.
10. Sanchez-Iglesias, A.; Pastoriza-Santos, I.; Perez-Juste, J.; Rodriguez-Gonzalez, B.; de Abajo, F. J. G.; Liz-Marzan, L. M. Synthesis and Optical Properties of Gold Nanodecahedra with Size Control. *Adv. Mater.* **2006**, *18*, 2529–2534.
11. Sun, Y. G.; Xia, Y. N. Shape-Controlled Synthesis of Gold and Silver Nanoparticles. *Science* **2002**, *298*, 2176–2179.
12. Turkevich, J.; Stevenson, P. C.; Hillier, J. A Study of the Nucleation and Growth Processes in the Synthesis of Colloidal Gold. *Discuss. Faraday Soc.* **1951**, *11*, 55–75.
13. Atwater, H. A.; Polman, A. Plasmonics for Improved Photovoltaic Devices. *Nat. Mater.* **2010**, *9*, 205–213.
14. Pillai, S.; Catchpole, K. R.; Trupke, T.; Green, M. A. Surface Plasmon Enhanced Silicon Solar Cells. *J. Appl. Phys.* **2007**, *101*, 093105.
15. Schaadt, D. M.; Feng, B.; Yu, E. T. Enhanced Semiconductor Optical Absorption *via* Surface Plasmon Excitation in Metal Nanoparticles. *Appl. Phys. Lett.* **2005**, *86*, 063106.
16. Stuart, H. R.; Hall, D. G. Absorption Enhancement in Silicon-on-Insulator Waveguides Using Metal Island Films. *Appl. Phys. Lett.* **1996**, *69*, 2327–2329.
17. Barnes, W. L.; Dereux, A.; Ebbesen, T. W. Surface Plasmon Subwavelength Optics. *Nature* **2003**, *424*, 824–830.
18. Ozbay, E. Plasmonics: Merging Photonics and Electronics at Nanoscale Dimensions. *Science* **2006**, *311*, 189–193.
19. Schuller, J. A.; Barnard, E. S.; Cai, W. S.; Jun, Y. C.; White, J. S.; Brongersma, M. L. Plasmonics for Extreme Light Concentration and Manipulation. *Nat. Mater.* **2010**, *9*, 193–204.
20. Baffou, G.; Quidant, R.; de Abajo, F. J. G. Nanoscale Control of Optical Heating in Complex Plasmonic Systems. *ACS Nano* **2010**, *4*, 709–716.
21. El-Sayed, I. H.; Huang, X. H.; El-Sayed, M. A. Surface Plasmon Resonance Scattering and Absorption of Anti-EGFR Antibody Conjugated Gold Nanoparticles in Cancer Diagnostics: Applications in Oral Cancer. *Nano Lett.* **2005**, *5*, 829–834.
22. Rosi, N. L.; Mirkin, C. A. Nanostructures in Biodiagnostics. *Chem. Rev.* **2005**, *105*, 1547–1562.
23. Zijlstra, P.; Chon, J. W. M.; Gu, M. Five-Dimensional Optical Recording Mediated by Surface Plasmons in Gold Nanorods. *Nature* **2009**, *459*, 410–413.
24. Camden, J. P.; Dieringer, J. A.; Wang, Y. M.; Masiello, D. J.; Marks, L. D.; Schatz, G. C.; Van Duyne, R. P. Probing the Structure of Single-Molecule Surface-Enhanced Raman Scattering Hot Spots. *J. Am. Chem. Soc.* **2008**, *130*, 12616–12617.
25. Stoerzinger, K. A.; Lin, J. Y.; Odom, T. W. Nanoparticle SERS Substrates with 3D Raman-Active Volumes. *Chem. Sci.* **2011**, *2*, 1435–1439.
26. Willets, K. A.; Van Duyne, R. P. Localized Surface Plasmon Resonance Spectroscopy and Sensing. *Annu. Rev. Phys. Chem.* **2007**, *58*, 267–297.
27. Michaels, A. M.; Nirmal, M.; Brus, L. E. Surface Enhanced Raman Spectroscopy of Individual Rhodamine 6G Molecules on Large Ag Nanocrystals. *J. Am. Chem. Soc.* **1999**, *121*, 9932–9939.
28. Talley, C. E.; Jackson, J. B.; Oubre, C.; Grady, N. K.; Hollars, C. W.; Lane, S. M.; Huser, T. R.; Nordlander, P.; Halas, N. J. Surface-Enhanced Raman Scattering from Individual Au Nanoparticles and Nanoparticle Dimer Substrates. *Nano Lett.* **2005**, *5*, 1569–1574.
29. Nie, S. M.; Emery, S. R. Probing Single Molecules and Single Nanoparticles by Surface-Enhanced Raman Scattering. *Science* **1997**, *275*, 1102–1106.
30. Alivisatos, P. The Use of Nanocrystals in Biological Detection. *Nat. Biotechnol.* **2004**, *22*, 47–52.
31. Anker, J. N.; Hall, W. P.; Lyandres, O.; Shah, N. C.; Zhao, J.; Van Duyne, R. P. Biosensing with Plasmonic Nanosensors. *Nat. Mater.* **2008**, *7*, 442–453.
32. Aers, G. C.; Inglesfield, J. E. Photoyield Enhancement from Small Metal Particles. *J. Phys. F Met. Phys.* **1983**, *13*, 1743–1756.
33. Endriz, J. G. Calculation of Surface Photoelectric Effect. *Phys. Rev. B* **1973**, *7*, 3464–3481.
34. Endriz, J. G.; Spicer, W. E. Experimental Evidence for Surface Photoelectric Effect in Aluminum. *Phys. Rev. Lett.* **1971**, *27*, 570–573.
35. Muller, U.; Burtscher, H.; Schmidt-Ott, A. Photoemission from Small Metal Spheres—A Model Calculation Using an Enhanced 3-Step Model. *Phys. Rev. B* **1988**, *38*, 7814–7816.
36. Levinson, H. J.; Plummer, E. W. The Surface Photoeffect. *Phys. Rev. B* **1981**, *24*, 628–638.
37. Barman, S. R.; Biswas, C.; Horn, K. Collective Excitations on Silver Surfaces Studied by Photoyield. *Surf. Sci.* **2004**, *566*, 538–543.
38. Pfeiffer, W.; Kennerknecht, C.; Merschdorf, M. Electron Dynamics in Supported Metal Nanoparticles: Relaxation

and Charge Transfer Studied by Time-Resolved Photoemission. *Appl. Phys. A-Mater. Sci. Process.* **2004**, *78*, 1011–1028.
39. Monchicourt, P.; Raynaud, M.; Saringar, H.; Kupersztych, J. Resonant Electron Emission of Silver Spheroids Induced by Laser Surface Plasmon Excitation. *J. Phys.-Condens. Matter* **1997**, *9*, 5765–5775.
40. Evers, F.; Rakete, C.; Watanabe, K.; Menzel, D.; Freund, H. J. Two-Photon Photoemission from Silver Nanoparticles on Thin Alumina Films: Role of Plasmon Excitation. *Surf. Sci.* **2005**, *593*, 43–48.
41. Kennerknecht, C.; Hovel, H.; Merschdorf, M.; Voll, S.; Pfeiffer, W. Surface Plasmon Assisted Photoemission from Au Nanoparticles on Graphite. *Appl. Phys. B, Lasers Opt.* **2001**, *73*, 425–429.
42. Lehmann, J.; Merschdorf, M.; Pfeiffer, W.; Thon, A.; Voll, S.; Gerber, G. Surface Plasmon Dynamics in Silver Nanoparticles Studied by Femtosecond Time-Resolved Photoemission. *Phys. Rev. Lett.* **2000**, *85*, 2921–2924.
43. Gloskovskii, A.; Valdaitsev, D. A.; Cinchetti, M.; Nepijko, S. A.; Lange, J.; Aeschlimann, M.; Bauer, M.; Klimenkov, M.; Viduta, L. V.; Tomchuk, P. M.; *et al.* Electron Emission from Films of Ag and Au Nanoparticles Excited by a Femtosecond Pump−Probe Laser. *Phys. Rev. B* **2008**, *77*, 195427.
44. Kubo, A.; Onda, K.; Petek, H.; Sun, Z. J.; Jung, Y. S.; Kim, H. K. Femtosecond Imaging of Surface Plasmon Dynamics in a Nanostructured Silver Film. *Nano Lett.* **2005**, *5*, 1123–1127.
45. Bormann, R.; Gulde, M.; Weismann, A.; Yalunin, S. V.; Ropers, C. Tip-Enhanced Strong-Field Photoemission. *Phys. Rev. Lett.* **2010**, *105*, 147601.
46. Kruger, M.; Schenk, M.; Hommelhoff, P. Attosecond Control of Electrons Emitted from a Nanoscale Metal Tip. *Nature* **2011**, *475*, 78–81.
47. Polyushkin, D. K.; Hendry, E.; Stone, E. K.; Barnes, W. L. THz Generation from Plasmonic Nanoparticle Arrays. *Nano Lett.* **2011**, *11*, 4718–4724.
48. Kim, S.; Jin, J.; Kim, Y.-J.; Park, I.-Y.; Kim, Y.; Kim, S.-W. High-Harmonic Generation by Resonant Plasmon Field Enhancement. *Nature* **2008**, *453*, 757–760.
49. Aeschlimann, M.; Bauer, M.; Bayer, D.; Brixner, T.; Cunovic, S.; Dimler, F.; Fischer, A.; Pfeiffer, W.; Rohmer, M.; Schneider, C.; *et al.* Spatiotemporal Control of Nanooptical Excitations. *Proc. Natl. Acad. Sci. U.S.A.* **2010**, *107*, 5329–5333.
50. Aeschlimann, M.; Brixner, T.; Fischer, A.; Kramer, C.; Melchior, P.; Pfeiffer, W.; Schneider, C.; Struber, C.; Tuchscherer, P.; Voronine, D. V. Coherent Two-Dimensional Nanoscopy. *Science* **2011**, *333*, 1723–1726.
51. Schweikhard, V.; Grubisic, A.; Baker, T. A.; Nesbitt, D. J. Multiphoton Scanning Photoionization Imaging Microscopy for Single-Particle Studies of Plasmonic Metal Nanostructures. *J. Phys. Chem. C* **2011**, *115*, 83–91.
52. Schweikhard, V.; Grubisic, A.; Baker, T. A.; Thomann, I.; Nesbitt, D. J. Polarization-Dependent Scanning Photoionization Microscopy: Ultrafast Plasmon-Mediated Electron Ejection Dynamics in Single Au Nanorods. *ACS Nano* **2011**, *5*, 3724–3735.
53. Hrelescu, C.; Sau, T. K.; Rogach, A. L.; Jackel, F.; Laurent, G.; Douillard, L.; Charra, F. Selective Excitation of Individual Plasmonic Hotspots at the Tips of Single Gold Nanostars. *Nano Lett.* **2011**, *11*, 402–407.
54. Cinchetti, M.; Gloskovskii, A.; Nepjiko, S. A.; Schonhense, G.; Rochholz, H.; Kreiter, M. Photoemission Electron Microscopy as a Tool for the Investigation of Optical Near Fields. *Phys. Rev. Lett.* **2005**, *95*, 047601.
55. Schertz, F.; Schmelzeisen, M.; Mohammadi, R.; Kreiter, M.; Elmers, H. J.; Schonhense, G. Near Field of Strongly Coupled Plasmons: Uncovering Dark Modes. *Nano Lett.* **2012**, *12*, 1885–1890.
56. Gloskovskii, A.; Valdaitsev, D.; Nepijko, S. A.; Schonhense, G.; Rethfeld, B. Coexisting Electron Emission Mechanisms in Small Metal Particles Observed in fs-Laser Excited PEEM. *Surf. Sci.* **2007**, *601*, 4706–4713.
57. Wiemann, C.; Bayer, D.; Rohmer, M.; Aeschlimann, M.; Bauer, M. Local 2PPE-Yield Enhancement in a Defined Periodic Silver Nanodisk Array. *Surf. Sci.* **2007**, *601*, 4714–4721.
58. Word, R. C.; Dornan, T.; Konenkamp, R. Photoemission from Localized Surface Plasmons in Fractal Metal Nanostructures. *Appl. Phys. Lett.* **2010**, *96*, 251110.
59. Douillard, L.; Charra, F.; Korczak, Z.; Bachelot, R.; Kostcheev, S.; Lerondel, G.; Adam, P. M.; Royer, P. Short Range Plasmon Resonators Probed by Photoemission Electron Microscopy. *Nano Lett.* **2008**, *8*, 935–940.
60. Meyer zu Heringdorf, F.; Buckanie, N. Nonlinear Photoemission Microscopy with Surface Plasmon Polaritons. *Microsc. Microanal.* **2010**, *16*, 502–503.
61. Petek, H.; Ogawa, S. Femtosecond Time-Resolved Two-Photon Photoemission Studies of Electron Dynamics in Metals. *Prog. Surf. Sci.* **1998**, *56*, 239–310.
62. Winkelmann, A.; Lin, W. C.; Chiang, C. T.; Bisio, F.; Petek, H.; Kirschner, J. Resonant Coherent Three-Photon Photoemission from Cu(001). *Phys. Rev. B* **2009**, *80*, 155128.
63. Bovensiepen, U.; Declair, S.; Lisowski, M.; Loukakos, P. A.; Hotzel, A.; Richter, M.; Knorr, A.; Wolf, M. Ultrafast Electron Dynamics in Metals: Real-Time Analysis of a Reflected Light Field Using Photoelectrons. *Phys. Rev. B* **2009**, *79*, 045415.
64. Bisio, F.; Nyvlt, M.; Franta, J.; Petek, H.; Kirschner, J. Mechanisms of High-Order Perturbative Photoemission from Cu(001). *Phys. Rev. Lett.* **2006**, *96*, 087601.
65. Ogawa, S.; Nagano, H.; Petek, H.; Heberle, A. P. Optical Dephasing in Cu(111) Measured by Interferometric Two-Photon Time-Resolved Photoemission. *Phys. Rev. Lett.* **1997**, *78*, 1339–1342.
66. Gudde, J.; Rohleder, M.; Meier, T.; Koch, S. W.; Hofer, U. Time-Resolved Investigation of Coherently Controlled Electric Currents at a Metal Surface. *Science* **2007**, *318*, 1287–1291.
67. Kruger, M.; Schenk, M.; Forster, M.; Hommelhoff, P. Attosecond Physics in Photoemission from a Metal Nanotip. *J. Phys. B* **2012**, *45*, 074006.
68. Ross, B. M.; Lee, L. P. Comparison of Near- and Far-Field Measures for Plasmon Resonance of Metallic Nanoparticles. *Opt. Lett.* **2009**, *34*, 896–898.
69. Messinger, B. J.; Vonraben, K. U.; Chang, R. K.; Barber, P. W. Local-Fields at the Surface of Noble-Metal Microspheres. *Phys. Rev. B* **1981**, *24*, 649–657.
70. Grady, N. K.; Halas, N. J.; Nordlander, P. Influence of Dielectric Function Properties on the Optical Response of Plasmon Resonant Metallic Nanoparticles. *Chem. Phys. Lett.* **2004**, *399*, 167–171.
71. Zuloaga, J.; Nordlander, P. On the Energy Shift between Near-Field and Far-Field Peak Intensities in Localized Plasmon Systems. *Nano Lett.* **2011**, *11*, 1280–1283.
72. Sonnichsen, C.; Franzl, T.; Wilk, T.; von Plessen, G.; Feldmann, J.; Wilson, O.; Mulvaney, P. Drastic Reduction of Plasmon Damping in Gold Nanorods. *Phys. Rev. Lett.* **2002**, *88*, 077402.
73. Link, S.; Mohamed, M. B.; El-Sayed, M. A. Simulation of the Optical Absorption Spectra of Gold Nanorods as a Function of their Aspect Ratio and the Effect of the Medium Dielectric Constant. *J. Phys. Chem. B* **1999**, *103*, 3073–3077.
74. Yalunin, S. V.; Gulde, M.; Ropers, C. Strong-Field Photoemission from Surfaces: Theoretical Approaches. *Phys. Rev. B* **2011**, *84*, 195426.
75. Ekici, O.; Harrison, R. K.; Durr, N. J.; Eversole, D. S.; Lee, M.; Ben-Yakar, A. Thermal Analysis of Gold Nanorods Heated with Femtosecond Laser Pulses. *J. Phys. D* **2008**, *41*, 185501.
76. Link, S.; El-Sayed, M. A. Shape and Size Dependence of Radiative, Non-radiative and Photothermal Properties of Gold Nanocrystals. *Int. Rev. Phys. Chem.* **2000**, *19*, 409–453.
77. Petrova, H.; Juste, J. P.; Pastoriza-Santos, I.; Hartland, G. V.; Liz-Marzan, L. M.; Mulvaney, P. On the Temperature Stability of Gold Nanorods: Comparison between Thermal and Ultrafast Laser-Induced Heating. *Phys. Chem. Chem. Phys.* **2006**, *8*, 814–821.
78. Novo, C.; Gomez, D.; Perez-Juste, J.; Zhang, Z. Y.; Petrova, H.; Reismann, M.; Mulvaney, P.; Hartland, G. V. Contributions from Radiation Damping and Surface Scattering to the Linewidth of the Longitudinal Plasmon Band of Gold

Nanorods: A Single Particle Study. *Phys. Chem. Chem. Phys.* **2006**, *8*, 3540–3546.
79. Keldysh, L. V. Ionization in Field of a Strong Electromagnetic Wave. *Sov. Phys. JETP-USSR* **1965**, *20*, 1307–1314.
80. Anisimov, S. I.; Benderskii, V. A.; Farkas, G. Nonlinear Photoelectric Effect in Metals Produced by a Laser-Radiation. *Usp. Fiziol. Nauk* **1977**, *122*, 185–222.
81. Bunkin, F. V.; Fedorov, M. V. Cold Emission of Electrons from Surface of a Metal in a Strong Radiation Field. *Sov. Phys. JETP-USSR* **1965**, *21*, 896–899.
82. Gladun, A. D.; Barashev, P. P. Multiquantum Photoemissive Effect. *Sov. Phys. Usp.* **1970**, *12*, 490–506.
83. Silin, A. P. Many-Photon Surface Photoelectric Effect in Metals. *Sov. Phys., Solid State* **1971**, *12*, 2886–2889.
84. Dushman, S. Thermionic Emission. *Rev. Mod. Phys.* **1930**, *2*, 0381–0476.
85. Herring, C.; Nichols, M. H. Thermionic Emission. *Rev. Mod. Phys.* **1949**, *21*, 185–270.
86. Richardson, O. W. *Emission of Electricity from Hot Bodies*; Longmans Green & Co.: London, 1921.
87. Guo, C. L.; Rodriguez, G.; Taylor, A. J. Ultrafast Dynamics of Electron Thermalization in Gold. *Phys. Rev. Lett.* **2001**, *86*, 1638–1641.
88. Elsayed-Ali, H. E.; Norris, T. B.; Pessot, M. A.; Mourou, G. A. Time-Resolved Observation of Electron-Phonon Relaxation in Copper. *Phys. Rev. Lett.* **1987**, *58*, 1212–1215.
89. Irvine, S. E.; Dechant, A.; Elezzabi, A. Y. Generation of 0.4-keV Femtosecond Electron Pulses Using Impulsively Excited Surface Plasmons. *Phys. Rev. Lett.* **2004**, *93*, 184801.
90. Kupersztych, J.; Monchicourt, P.; Raynaud, M. Ponderomotive Acceleration of Photoelectrons in Surface-Plasmon-Assisted Multiphoton Photoelectric Emission. *Phys. Rev. Lett.* **2001**, *86*, 5180–5183.
91. Raynaud, M.; Kupersztych, J. Ponderomotive Effects in the Femtosecond Plasmon-Assisted Photoelectric Effect in Bulk Metals: Evidence for Coupling between Surface and Interface Plasmons. *Phys. Rev. B* **2007**, *76*, 241402.
92. Michaelson, H. B. Work Function of Elements and Its Periodicity. *J. Appl. Phys.* **1977**, *48*, 4729–4733.
93. Schlaf, R.; Murata, H.; Kafafi, Z. H. Work Function Measurements on Indium Tin Oxide Films. *J. Electron Spectrosc. Relat. Phenom.* **2001**, *120*, 149–154.
94. Monti, O. L. A.; Baker, T. A.; Nesbitt, D. J. Imaging Nanostructures with Scanning Photoionization Microscopy. *J. Chem. Phys.* **2006**, *125*, 154709.
95. Henry, A. I.; Bingham, J. M.; Ringe, E.; Marks, L. D.; Schatz, G. C.; Van Duyne, R. P. Correlated Structure and Optical Property Studies of Plasmonic Nanoparticles. *J. Phys. Chem. C* **2011**, *115*, 9291–9305.
96. Encina, E. R.; Coronado, E. A. Resonance Conditions for Multipole Plasmon Excitations in Noble Metal Nanorods. *J. Phys. Chem. C* **2007**, *111*, 16796–16801.
97. Slaughter, L. S.; Chang, W. S.; Swanglap, P.; Tcherniak, A.; Khanal, B. P.; Zubarev, E. R.; Link, S. Single-Particle Spectroscopy of Gold Nanorods beyond the Quasi-static Limit: Varying the Width at Constant Aspect Ratio. *J. Phys. Chem. C* **2010**, *114*, 4934–4938.
98. Johnson, P. B.; Christy, R. W. Optical-Constants of Noble-Metals. *Phys. Rev. B* **1972**, *6*, 4370–4379.